RSC Advances

PAPER

View Article Online
View Journal | View Issue

Cite this: *RSC Adv.*, 2023, **13**, 1594

Visible-light driven p–n heterojunction formed between α-Bi_2O_3 and $Bi_2O_2CO_3$ for efficient photocatalytic degradation of tetracycline†

Baikang Zhu,‡[abd] Qinbing Dong,‡[a] Jianghua Huang,‡[a] Debin Song,[a] Lihui Chen,[a] Qingguo Chen,[a] Chunyang Zhai,[c] Bohong Wang,*[a] Jiří Jaromír Klemeš*[e] and Hengcong Tao*[adf]

To improve the efficiency of photocatalytic oxidative degradation of antibiotic pollutants, it is essential to develop an efficient and stable photocatalyst. In this study, a polymer-assisted facile synthesis strategy is proposed for the polymorph-controlled α-Bi_2O_3/$Bi_2O_2CO_3$ heterojunction retained at elevated calcination temperatures. The p–n heterojunction can effectively separate and migrate electron–hole pairs, which improves visible-light-driven photocatalytic degradation from tetracycline (TC). The BO-400@PAN-140 photocatalyst achieves the highest pollutant removal efficiency of 98.21% for photocatalytic tetracycline degradation in 1 h (λ > 420 nm), and the degradation efficiency was maintained above 95% after 5 cycles. The morphology, crystal structure, and chemical state of the composites were analysed by scanning electron microscopy, X-ray diffraction, and X-ray photoelectron spectroscopy. Ultraviolet-visible diffuse reflection, transient photocurrent response, and electrochemical impedance spectroscopy were adopted to identify the charge transfer and separation efficiency of photogenerated electron–hole pairs. The EPR results verified h^+ and $^{\bullet}OH$ radicals as the primary active species in the photocatalytic oxidation reactions. This observation was also consistent with the results of radical trapping experiments. In addition, the key intermediate products of the photocatalytic degradation of TC over BO-400@PAN-140 were identified *via* high-performance liquid chromatography-mass spectrometry, which is compatible with two possible photocatalytic reaction pathways. This work provides instructive guidelines for designing heterojunction photocatalysts *via* a polymer-assisted semiconductor crystallographic transition pathway for TC degradation into cleaner production.

Received 22nd December 2022
Accepted 26th December 2022

DOI: 10.1039/d2ra08162h

rsc.li/rsc-advances

Introduction

In recent years, with the development of industrialization in the world, wastewater pollution is becoming more and more serious. The type of pollutants in the water also exhibit a trend of diversification.[1] Emerging antibiotic pollutants, which are considered hazardous to the ecosystem, are prevalent in surface water, groundwater, and wastewater treatment plant effluents.[2] Among them, tetracycline has often been reported as the most famous broad-spectrum antibacterial agent and antibiotic pollutants in water.[3] However, the degradation of tetracycline in wastewater is difficult. Conventional wastewater treatment technologies (chlorine, ozone, filtration, and adsorption) have the disadvantages of high cost, complex processes, limited purification effect, and secondary pollution.[4] Therefore, it is imperative to develop technologies to effectively reduce the elimination of such antibiotics.[5]

Photocatalysis has attracted significant interest owing to its non-pollution, safety, and other characteristics for addressing environmental pollution.[6–8] It can degrade organic pollutants in water into carbon dioxide and water. In addition, the photocatalyst used is non-toxic, low-cost, stable and reusable.[9] Up to now, efforts have been made to develop photocatalysts that use visible light to efficiently remove tetracycline.[10]

[a]*School of Petrochemical Engineering & Environment, Zhejiang Ocean University, Zhoushan, 316022, China. E-mail: hengcongtao@zjou.edu.cn*

[b]*United National-Local Engineering Laboratory of Oil & Gas Storage and Transportation Technology, Zhoushan, Zhejiang, 316022, China*

[c]*School of Materials Science and Chemical Engineering, Ningbo University, Ningbo 315211, China*

[d]*Zhejiang Provincial Key Laboratory of Petrochemical Environmental Pollution Control, Zhoushan, Zhejiang, 316022, China*

[e]*Sustainable Process Integration Laboratory – SPIL, NETME Centre, Faculty of Mechanical Engineering, Brno University of Technology – VUT Brno, Technická 2896/2, 616 69, Brno, Czech Republic*

[f]*College of Chemical and Biological Engineering, Zhejiang University, Hangzhou, 310058, China*

† Electronic supplementary information (ESI) available. See DOI: https://doi.org/10.1039/d2ra08162h

‡ These authors contributed equally to this work.

Bismuth-based photocatalysts (such as Bi_2O_3, $Bi_2O_2CO_3$, and Bi_2WO_6) are considered highly favourable candidates for environmental remediation applications owing to their relatively high visible light absorption capacities.[11] Notably, α-Bi_2O_3 exhibits excellent photodegradation activity (owing to its favourable bandgap energy structure and efficient photoelectric transformation rate) toward organic pollutants, including Rhodamine B (RhB),[12] 2,4-DCP,[13] tetracycline (TC).[14] The unique layered structure of n-type $Bi_2O_2CO_3$ consists of alternating perovskite-like slabs of CO_3^{2-} and layers of $(Bi_2O_2)^{2+}$ to promote photogeneration while also exploiting a limited area of the UV light region.[14–16] However, the inefficient utilisation of sunlight and the fast combination rate of photogeneration significantly constrain the degradation activity of $Bi_2O_2CO_3$ [17] and the construction of a heterojunction is crucial to impeding the recombination rate of photogenerated electron–hole pairs and enhance photocatalytic performance.

In contrast with pure n-type photocatalysts, the generation of an interior electric field between the n-type and p-type semiconductors of the p–n heterojunction effectively drives the photogenerated charge transfer and separation.[18] As a result, the rational bandgap structure of the p–n heterojunction photocatalysts increases the lifetime of the carrier while also preserving the threshold energy level of the photoelectron. Various studies have reported the heterojunction of Bi-based materials, such as $Bi_2O_2CO_3$/g-C_3N_4 heterojunctions for sulfamethazine degradation[19] and Bi_2O_3/g-C_3N_4 nanocomposites for amido black 10B degradation. Relative to β-Bi_2O_3, α-Bi_2O_3 possesses the advantages of a smaller bandgap, higher oxidative ability of the valence hole, and non-toxicity.[20,21] Traditional methods to prepare Bi_2O_3/$Bi_2O_2CO_3$ heterojunction photocatalysts are based on heat treatment strategies. In the calcination process, when the calcination temperature reaches about 350 °C, $Bi_2O_2CO_3$ firstly decomposes to form β-Bi_2O_3, and then transforms from β-Bi_2O_3 to α-Bi_2O_3 by continuing to increase the calcination temperature. At present, the main research is the formation of β-Bi_2O_3/$Bi_2O_2CO_3$ and β-Bi_2O_3/α-Bi_2O_3 heterostructure, α-Bi_2O_3/$Bi_2O_2CO_3$ heterostructure is relatively difficult to achieve. Which are relatively difficult to implement for the successful formation of the $Bi_2O_2CO_3$/α-Bi_2O_3 heterostructure. For this reason, the use of α-Bi_2O_3/$Bi_2O_2CO_3$ heterojunction materials in photocatalytic degradation of pollutants has rarely been reported.

Researchers have recently succeeded in implementing the controlled synthesis of photocatalysts through the introduction of polymers as structure-directing agents to control the type of crystal growth.[22,23] Various polymers with specific functional groups have been utilised owing to their superior ability to anchor with metal ions.[24,25] Polyacrylonitrile (PAN) has been widely utilised for such controllable syntheses.[26] The introduction of small quantities of polymer to the system acts as a protection for partial nanoparticles by enabling them to retain their original crystalline morphology at elevated temperatures.

In this paper, a simple polymer-assisted synthesis method is developed based on the introduction of PAN, thereby enabling the formation of α-Bi_2O_3/$Bi_2O_2CO_3$ heterostructure directly obtained from $Bi_2O_2CO_3$ through partial transformation. The $Bi_2O_2CO_3$ precursor was synthesised through the hydrothermal method. The polymer, PAN, was specified as the capping agent to envelop the partial $Bi_2O_2CO_3$ precursor. In addition, TC and RhB were adopted as the representative target pollutants to assess the photocatalytic properties of the α-Bi_2O_3/$Bi_2O_2CO_3$ heterostructure photocatalyst. This work provides deep insight and a promising strategy to design highly efficient hybrid photocatalysts for environmental remediation.

Experimental section

Chemicals

Ethylenediaminetetraacetate dihydrate (EDTA), bismuth nitrate pentahydrate ($Bi(NO_3)_3 \cdot 5H_2O$), citric acid ($C_6O_7H_8$), TBA, polyacrylonitrile (PAN, average molecular weight 150 000), and L-ascorbic acid (L-AA) were purchased from Aladdin Reagent Co., Ltd (Shanghai, China). Nitric acid (HNO_3), sodium hydroxide (NaOH), disodium, anhydrous ethanol (C_2H_5OH), sodium sulfate (Na_2SO_4), and *N*,*N*-dimethylformamide (DMF) were purchased from Shanghai Chemical Reagent Company (Shanghai, China). All chemicals were utilised without purification.

Synthesis of $Bi_2O_2CO_3$

The $Bi_2O_2CO_3$ was prepared by a simple hydrothermal method. First, 6 mmol of $Bi(NO_3)_3 \cdot 5H_2O$ were dissolved into 30 mL of nitric acid (1 M) in a 100 mL round-bottomed flask. 2 mmol citric acid was then dissolved into the solution and vigorously stirred for 10 min. 2 M NaOH aqueous solution was slowly dropped into the solution to adjust the pH value to 4. The mixture was heated at 180 °C for 24 h after having transferred to a 100 mL hydrothermal autoclave. The subsequent white precipitate was centrifuged and rinsed with deionised water/absolute ethanol three times. The final $Bi_2O_2CO_3$ sample was obtained by drying the precipitate in a vacuum for 12 h at 60 °C (denoted as BO). Samples of BO were calcinated in a covered square crucible and heated at intervals of 3 °C min^{-1} to 250–500 °C; the sample was then kept for 2 h in an atmosphere of hydrogen. The calcinated samples were denoted as BO-*X* (X = 250, 300, 350, 400, 450, and 500 °C) consistent with the specific calcination temperature.

Synthesis of BO-*X*@PAN-*Y*

10 mg of PAN were added to 25 mL of DMF. A given mass (corresponding to $M_{PAN} : M_{BO\text{-}X} = 1:10, 1:100, 1:140, 1:180$) of BO-*X* was then dispersed into this solution with 4 h of stirring followed by ultrasonication for 1 h. The mixed solution was desiccated at 150 °C for 12 h to evaporate the *N*,*N*-dimethylformamide. The final nanocomposite was prepared by calcining the mixture at 350, 400, and 450 °C for 2 h in an N_2 atmosphere. The prepared samples were denoted as BO-*X*@PAN-*Y* (Y = 10, 100, 140, 180) consistent with the mass ratio of PAN to BO-*X*.

Characterisations

XRD (DX-2700, China) with Cu-Kα radiation ($\lambda = 0.15406$ Å) was employed to investigate the crystalline phases in the 2θ region from 10° to 80° with the operating parameters of 40 kV and 150 mA. Images of the sample morphology were obtained *via* SEM (Zeiss Sigma 300, Germany) and TEM (FEI Tecnai G2 F20, Netherland). The chemical properties and structure of the catalyst surface were characterised by XPS (Thermo Scientific K-Alpha, USA) with Al Kα X-ray ($h\nu$ – 1486.6 eV) radiation. The binding energy was calibrated with C 1s = 284.50 eV as the reference. TGA was carried out using a thermal gravimetric analyser (TGA5500, USA) at 10.0 °C min^{-1} under a N_2 atmosphere (10 mL min^{-1}). UV-vis DRS were obtained using a UV-2600 (Shimadzu, Japan) and with $BaSO_4$ as a reference. The electrochemical workstation (CHI 660E, Shanghai Chenhua, China) was used to detect the TPR (I–t plots) with a conventional three-electrode configuration in a square quartz electrolytic cell under radiation by a 300 W Xe lamp at 20 s intervals. EIS was conducted with the conventional three-electrode system and recorded over a frequency range of 0.01 Hz–10^5 Hz with an AC amplitude of 50 mV. Gauze platinum and silver chloride electrodes functioned as counter electrodes in the conventional three-electrode system. 0.5 M sodium sulfate solution was utilised as the electrolyte for the TPR. The mixed solution of potassium ferricyanide (0.1 M), potassium ferrous cyanide (0.1 M) and potassium chloride (0.1 M) was used as the electrolyte for electrochemical impedance experiments. Photoluminescence (PL) emission spectra were generated using the fluorescence spectrophotometer (FSL1000, Edinburgh Instruments Ltd, United Kingdom). The ESR signals of active species were collected on a spectrometer (Bruker EMXPLUS, Germany). Hydroxyl radicals ($^{\bullet}OH$) and positive holes (h^+) were detected by dispersing the samples in a 50 mM solution of 5,5-dimethyl-1-pyrroline N-oxide (DMPO) under visible-light illumination ($\lambda >$ 420 nm).

Photocatalytic activity test

The photocatalytic performance of the catalysts was estimated after removing TC or RhB from water. A 300 W Xenon lamp with a 420 nm pass filter was adopted as the light source. 50 mg of the prepared samples were dispersed in a quartz glass reactor containing 100 mL of aqueous TC (30 mg L^{-1}) or RhB (30 mg L^{-1}) water solution. The experimental temperature was controlled at room temperature by a circulating water bath system. To reach adsorption–desorption equilibrium, the mixture was continuously stirred in the dark for 30 min prior to photocatalysis. During irradiation, the reaction solution (5 mL) was sampled (5 mL of suspension) at fixed time intervals. The catalyst was removed by filtration through a hydrolases syringe filter (0.22 μm). The concentrations of TC and RhB were evaluated by UV-vis spectrophotometer (TU-1901, Persee, China). The characteristic absorption peaks of TC at RhB (357 and 554 nm, respectively) were used to quantify the extent of degradation. The removal rate (η) of the photocatalyst was calculated from eqn (1):

$$\eta\ (\%) = (1 - C/C_0) \times 100\% \quad (1)$$

The concentrations of filtrates before and after irradiation are represented by the symbols C_0 and C, respectively.

The oxidation intermediate TC degradation products were measured by HPLC-MS (Agilent 1100 series, USA). The mobile phase employed a mixture of acetonitrile and formic acid (0.1%) with a flow rate of 0.135 mL min^{-1} (injection volume and mass range: 5.0 μL and 50–500 m/z, respectively; fragment and capillary voltage: 130 and 2800 V, respectively). Various trapping agents were added prior to the photocatalytic reaction to detect the existence of active free radicals.

Results and discussion

Structures and compositions of photocatalysts

$Bi_2O_2CO_3$ and modified $Bi_2O_2CO_3$ precursors were first synthesised using a facile hydrothermal method. The photocatalyst synthetic process is illustrated in Scheme 1. As shown in Fig. 1, the crystal structures of the $Bi_2O_2CO_3$, β-Bi_2O_3, pure α-Bi_2O_3, $Bi_2O_2CO_3$/β-Bi_2O_3, α-Bi_2O_3/β-Bi_2O_3, and $Bi_2O_2CO_3$/α-Bi_2O_3 powders were analysed by XRD. Fig. 1a illustrates the XRD patterns of the $Bi_2O_2CO_3$ precursor prior to polymer modification and annealing at various temperatures. At calcination temperatures less than 250 °C, all the BO-250 diffraction peaks corresponded to the $Bi_2O_2CO_3$ crystal planes (JCPDS no. 41-1488).[27] Annealing at temperatures between 250 and 300 °C decoupled the C–O bonds of $Bi_2O_2CO_3$ corresponding to the gradual reduction of carbon elements and the conversion of $Bi_2O_2CO_3$ to β-Bi_2O_3. When the calcination temperature was increased to 350 °C, a more prominent β-Bi_2O_3 peak appeared ($2\theta = 27.90°$) (JCPDS no. 27-0050), suggesting a considerable increase in the β-Bi_2O_3 content in the composite. α-Bi_2O_3 manifested at 400 °C (JCPDS no. 71-2274), while at approximately 500 °C, the β-Bi_2O_3 crystal evolved into α-Bi_2O_3 following the rupture of double Bi_2O_3=Bi_2O_3 bonds.[28] The introduction of the polymer was also associated with comparable transitions in the crystal morphology with temperature (Fig. 1b). The observations of BO-400@PAN-140 indicated that the diffraction peak of $Bi_2O_2CO_3$ at $2\theta = 30.251°$ reappeared after the polymer was added. Fig. 1c and d present the influence of the polymer to precursor ratio. The diffraction peak intensity of $Bi_2O_2CO_3$ gradually enhanced with the upsurge of the polymer ratio, which may be caused by PAN coating on the outside of $Bi_2O_2CO_3$ to protect $Bi_2O_2CO_3$ from transformation during calcination,

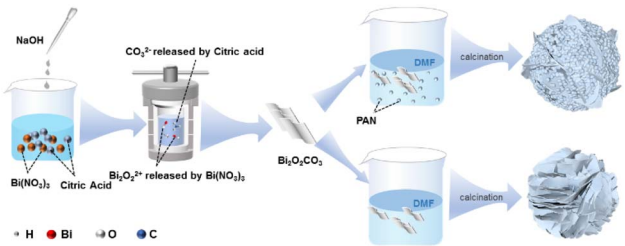

Scheme 1 Schematic diagram of sample synthesis.

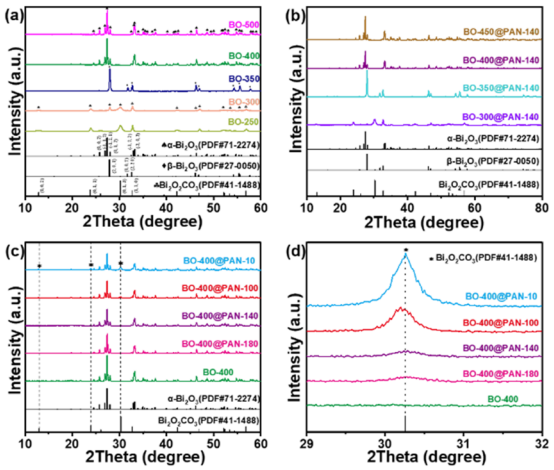

Fig. 1 XRD patterns of (a) the $Bi_2O_2CO_3$ precursors and (b) polymer-modified $Bi_2O_2CO_3$ precursors were calcined at various temperatures. (c and d) Polymer-modified $Bi_2O_2CO_3$ with various molar ratios (polymer/$Bi_2O_2CO_3$) calcined at 400 °C.

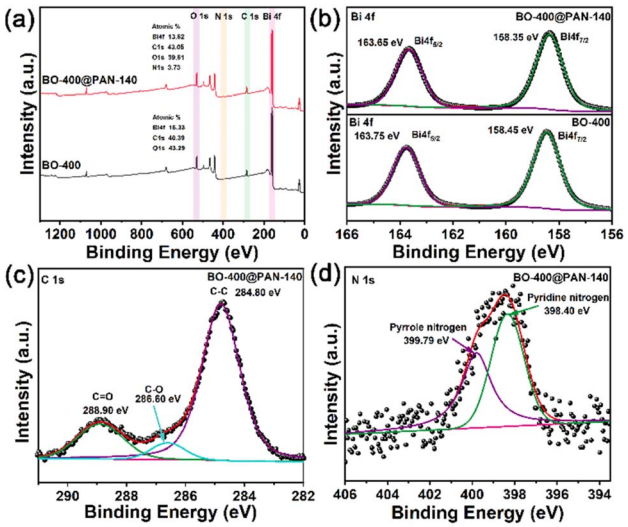

Fig. 2 X-ray photoelectron spectroscopy (XPS) survey spectra: (a) high-resolution XPS spectra of Bi 4f; (b) BO-400 and BO-400@PAN-140 and C 1s (c); N 1s; (d) BO-400@PAN-140.

while also indicating the formation of an α-Bi_2O_3/$Bi_2O_2CO_3$ heterojunction (Fig. S1†).

Thermogravimetric analysis (TGA) analyses were performed to further quantify the phase transformation behaviour during the precursor calcination process.[29] Fig. S2† presents a relatively wide endothermal temperature range from 100 to 270 °C, with the highest peak emerging at 335 °C and a comparatively steady, stage-based performance between 270 and 320 °C. This phase transformation behaviour is consistent with the XRD results; for example, the $Bi_2O_2CO_3$ precursor is converted in a piecemeal manner to $Bi_2O_2CO_3$/β-Bi_2O_3 and pure β-Bi_2O_3 at a specific intermediate temperature because of the thermal decomposition. β-Bi_2O_3 is then converted to β-Bi_2O_3/α-Bi_2O_3 and α-Bi_2O_3 following calcination at higher temperatures.

XPS analyses were further conducted to investigate the surface chemical components and the elemental states. The survey spectra of BO-400 and BO-400@PAN-140 (Fig. 2a) indicate the presence of C, O, Bi, and N on the material surface. In Fig. S3,† the two peaks in the O 1s spectrum of BO-400@PAN-140 with binding energies at 530.70 and 529.11 eV correspond to metal carbonate and metal oxide, respectively. The N element is derived from the PAN molecules, while the C element of BO-400 originates from adventitious elemental carbon (Fig. S4†). The peak positioned at 288.90 eV is likely the result of carbon dioxide from the environment. In Fig. 2b, the two peaks in the Bi 4f spectrum of BO-400@PAN-140 with binding energies at 163.65 and 158.35 eV correspond to Bi $4f_{5/2}$ and Bi $4f_{7/2}$ of Bi^{3+}, respectively.[30,31]

In addition, the two peaks at 163.75 and 158.45 eV of Bi 4f are related to BO-400. In Fig. 2c, the C 1s spectra of BO-400@PAN-140 can be deconvoluted into three components at approximately 284.80, 286.60, and 288.90 eV. The peak consigned to 284.80 eV is associated with the C–C bonds of polyacrylonitrile, while the peak at approximately 286.60 eV results from the C–O of the adventitious carbon species. Finally, the peak near 288.90 eV corresponds to C=O, which is attributed to CO_3^{2-} in $Bi_2O_2CO_3$. Fig. S5† presents the X-ray photoelectron spectroscopy (XPS) spectra of the carbon element following the introduction of the polymer and prior to calcination. The BOC@PAN-140 peak located at 286.30 eV persists and is unaffected by the association with BO-400@PAN-140. The BO-400@PAN-140C 1s binding energy at 288.90 eV demonstrates an obvious blue shift relative to BOC@PAN-140, which is likely attributed to the alteration of the chemical bond energy between the bismuth atom and surface carbon species of $Bi_2O_2CO_3$ the latter corresponding to the adventitious carbon. The emergence of the carbonate peak indicates that the polymer inhibits the transition of bismuth oxycarbonate to bismuth oxide in a high-temperature environment. As shown in Fig. 2d, the N1 s peaks at 398.40 and 399.79 eV can be ascribed to C–N and C=N in BO-400@PAN-140.[32]

Fig. 3a–c presents the scanning electron microscopy (SEM) images of the surface morphologies of $Bi_2O_2CO_3$, BO-400@PAN-140, and BO-400@PAN-10. $Bi_2O_2CO_3$ can be seen to possess a layered structure with excellent structural homogeneity (Fig. 3a). As shown in Fig. S6a,† heating the $Bi_2O_2CO_3$ to 300 °C results in the aggregation of these nanosheets partially transforming them into nanometer-scale microspheres. Synthesizing this finding with the XRD data analysis, it is conjectured that these nanospheres are β-Bi_2O_3. Fig. S6b† indicates that the lateral size of the nanosheet decreases following the introduction of PAN. A small number of tiny nanospheres are present between the nanosheet layers, deriving from the partial inhibition of the transformation from $Bi_2O_2CO_3$ to β-Bi_2O_3. As shown in Fig. 3b, the partial nanosheets were transformed into unique dendritic structures. The transformation from $Bi_2O_2CO_3$ to α-Bi_2O_3 is the result of a solid reaction process.[33] The as-produced grain boundary presents a plausible reactive site for thermal decomposition. As a result of the polymer additive, the coated $Bi_2O_2CO_3$ transformed the α-Bi_2O_3/$Bi_2O_2CO_3$

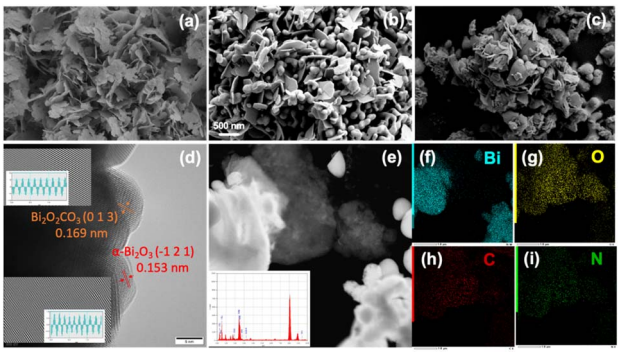

Fig. 3 Scanning electron microscopy (SEM) images of (a) $Bi_2O_2CO_3$, (b) BO-400@PAN-140, and (c) BO-400@PAN-10. Transmission electron microscopy (TEM) images of (d) BO-400@PAN-140. (e) Elemental dispersive spectroscopic (EDS) mapping profiles of (f) Bi, (g) O, (h) C, and (i) N.

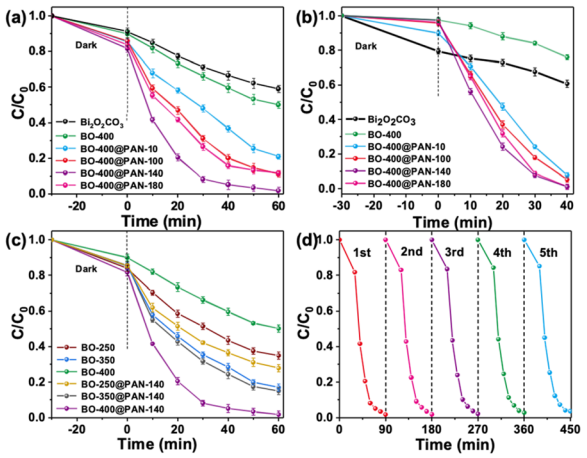

Fig. 4 (a) Photocatalytic degradation curves of TC under visible-light irradiation (λ > 420 nm) with BO-400@PAN-*Y* (*Y* = 10, 100, 140, 180). (b) Photocatalytic degradation curves of RhB under visible-light irradiation (λ > 420 nm) with BO-400@PAN-*Y* (*Y* = 10, 100, 140, 180). (c) Photocatalytic degradation curves of TC with samples synthesised at various calcination temperatures. (d) The cycling runs in the photodegradation of TC over BO-400@PAN-140 composites.

heterostructure at 400 °C. In addition, the mixing ratio of the polymer and $Bi_2O_2CO_3$ was found to significantly influence the final morphology of the photocatalyst. As shown in Fig. 3c, the extent of catalyst agglomeration increased with the polymer ratio. A mass ratio of $Bi_2O_2CO_3$ to PAN of 1 : 10 corresponded to the formation of a dendritic microsphere surface scattered with small, irregular flakes. Reducing this mass ratio to 1 : 100 led to the formation of smaller dendritic structures with stacked nanosheets (Fig. S6c†). As shown in Fig. S6d,† a mass ratio of $Bi_2O_2CO_3$ to PAN of 180 : 1 resulted in a significant increase in the number of dendritic structures formed. Simultaneously, the small number of lamellar structures can be attributed to the inhibition of bismuth oxycarbonate transformation. A representative high-resolution transmission electron microscopy (HR-TEM) image of the BO-400@PAN-140 sample is shown in Fig. 3d, in which the shaded area indicated by the yellow arrow is $Bi_2O_2CO_3$. The degree of lattice spacing between $Bi_2O_2CO_3$ nanosheets is consistent with the (013) spacing of the $Bi_2O_2CO_3$ phase. The α-Bi_2O_3 phase is indicated by the pink arrow; the degree of lattice spacing in this region is consistent with crystal planes of α-Bi_2O_3 (200). These visualisations confirm that the BO-400@PAN-140 sample possesses a demonstrable heterostructure with a well-contacted interface.[34] As shown in Fig. 3e, the EDS (elemental dispersive spectroscopic) mapping of composite BO-400@PAN-140 was obtained for the same region of the sample. The sample was found to be composed of bismuth, oxygen, carbon, and nitrogen—further confirming the presence of the two phases which comprise the targeted heterostructure. The distributions of the elements presented in Fig. 3f–i confirm the presence and even distribution of all four elements from each of the two phases.

Photocatalytic activity

The photocatalytic degradation performance of the synthesised catalysts, with respect to both TC and RhB, was evaluated under visible-light radiation. Fig. 4 presents the photodegradation of TC (as followed by its change in concentration) as a function of time. As shown in Fig. 4a, the degradation rate of TC catalysed solely by $Bi_2O_2CO_3$ and BO-400 was extremely slow compared to that which can be achieved in the presence of a polymer additive. $Bi_2O_2CO_3$ and BO-400 was associated with a TC removal efficiency of 40.9% and 49.84% within 60 min. As expected, the composites calcined at 400 °C exhibited an improved photocatalytic decomposition efficiency when compared with the conventional BO-400. Among these calcined samples, BO-400@PAN-140 possessed the highest photocatalytic performance (98.20%) for the degradation of TC within 60 min, which is 48.36% higher than that of BO-400. This increased photocatalytic activity may be attributed to the various crystal morphologies of $Bi_2O_2CO_3$ derived Bi_2O_3. The introduction of PAN inhibits the conversion of $Bi_2O_2CO_3$ to Bi_2O_3. The resulting $Bi_2O_2CO_3$/α-Bi_2O_3 heterojunction supports enhanced redox reaction. However, the degradation efficiency of TC decreased from 98.20 to 79.07% when the mass ratio of PAN was increased from 1 : 140 to 1 : 10 indicating that excessive PAN negatively impacts the photocatalytic degradation efficiency. Increased PAN may result in catalyst agglomeration, thereby limiting the contact area of the catalyst available to the pollutant. The TC removal efficiency of BO-400@PAN-10, BO-400@PAN-100, and BO-400@PAN-180 (within 60 min) were 79.07, 88.75, and 88.26%, respectively. The rate constant of the kinetic fitting curves (Fig. S7†) for $Bi_2O_2CO_3$, BO-400, BO-400@PAN-10, BO-400@PAN-100, BO-400@PAN-140, and BO-400@PAN-180 were 0.00633, 0.01009, 0.02371, 0.03455, 0.06358, and 0.03476 min^{-1}, respectively. The TC degradation rate constant over the α-Bi_2O_3/$Bi_2O_2CO_3$ heterojunction is nearly 6.3 times higher than over pure α-Bi_2O_3. Remarkably, the photocatalytic degradation activity of BO-400@PAN-140 was enhanced to levels comparable to the previously referenced best-in-class photocatalysts (Table 1). As shown in Fig. 4b, BO-400@PAN-140 can also enable the efficient photodegradation of RhB. The trend of RhB photodegradation efficiency with the PAN content of the

Table 1 Photocatalytic degradation of TC by various photocatalysts

Photocatalysts	Light source	Dosage	Volume and concentration	Degradation efficiency	Ref.
$CeO_2/C/Bi_2O_2CO_3$	Visible light	35 mg	100 mL; 20 mg L^{-1}	79.5% (90 min)	35
$AgBr/5GO/Bi_2WO_6$	Visible light	40 mg	100 mL; 20 mg L^{-1}	84% (60 min)	34
$BiOCl_{0.9}I_{0.1}/\beta\text{-}Bi_2O_3$	Simulated sunlight	20 mg	50 mL; 20 mg L^{-1}	82.4% (120 min)	36
$OVs\text{-}BiOI/\alpha\text{-}Bi_2O_3$	Visible light	50 mg	50 mL; 20 mg L^{-1}	84% (120 min)	37
$\beta\text{-}Bi_2O_3/Bi_2O_2CO_3$	Simulated sunlight	100 mg	100 mL; 30 mg L^{-1}	93.79% (60 min)	21
BO-400@PAN-140 ($\alpha\text{-}Bi_2O_3/Bi_2O_2CO_3$)	Visible light	30 mg	100 mL; 30 mg L^{-1}	98.20% (60 min)	This work

photocatalyst is similar to that for TC. BO-400@PAN-140 possesses the highest photocatalytic performance (98.91%) for the degradation of RhB in 40 min. BO-400@PAN-10, BO-400@PAN-100, and BO-400@PAN-180 enabled the effective degradation of more than 90% of RhB within 40 min of visible-light illumination, compared to that by the original BO-400 (24.02%) and $Bi_2O_2CO_3$ (39.7%).

The rate of TC degradation was further investigated in relation to the calcination temperature of the photocatalyst (Fig. 4c). The catalyst calcination temperatures of 250, 350, and 400 °C corresponded to TC decomposition rates of 65.17, 83.10, and 49.84%, respectively, in the absence of the PAN additive. The decline in catalyst performance at elevated calcination temperatures may be understood in terms of the evolution of its crystal morphology *i.e.*, the complete conversion of $Bi_2O_2CO_3$ to $\beta\text{-}Bi_2O_3$ at 350 °C, while transforming completely into $\alpha\text{-}Bi_2O_3$ 400 °C. The decomposition rates of TC achieved by BO-250@PAN-140, BO-350@PAN-140, and BO-400@PAN-140 were 72.19, 83.10, and 98.20%, based on a constant PAN mass ratio (1 : 140). The introduction of PAN inhibited the partial transformation of $Bi_2O_2CO_3$ into $\alpha\text{-}Bi_2O_3$ at elevated calcination temperatures, while the heterojunction formed by $Bi_2O_2CO_3$ and $\alpha\text{-}Bi_2O_3$ improved the catalytic efficiency. As shown in Fig. S8,† the kinetic fitting curve rate constants for BO-250, BO-350, BO-400, BO-250@PAN-140, BO-350@PAN-140, and BO-400@PAN-140 were 0.01498, 0.02665, 0.01009, 0.01816, 0.02896, and 0.06358 min^{-1}, respectively. BO-400@PAN-140 exhibits the highest apparent rate constant, which is approximately 4.2, 2.4, 6.3, 3.5, and 2.2 times higher than those of BO-250, BO-350, BO-400, BO-250@PAN-140, BO-350@PAN-140, and BO-400@PAN-180, respectively. The experiments were repeated over five cycles under controlled visible-light irradiation to validate the reproducibility of the results.[38] The degradation rate of TC was maintained above 95% in each cycle (Fig. 4d). Out of all the possible permutations of PAN composition and calcination temperatures, BO-400@PAN-140 exhibited the most superior photocatalytic degradation performance in terms of both activity and stability. Fig. S9† clearly indicated that the prepared composites BO-400@PAN-140 shows a 45% mineralisation efficiency of TC within 100 min visible light irritation. This result confirmed that BO-400@PAN-140 could mineralise TC into intermediate compounds or CO_2 and H_2O.

Optical properties

As established in previous studies, both light absorption characteristics and energy band features are critical to the performances of the photocatalysts.[39] Fig. 5a presents the UV-vis diffuse reflectance spectra of the $Bi_2O_2CO_3$, BO-400, and BO-400@PAN-140 photocatalysts. $Bi_2O_2CO_3$ was found to absorb UV light limited by absorption edge at 390 nm. In contrast, BO-400, and BO-400@PAN-140 can absorb wavelengths in the visible-light region indicating their suitability for visible-light-driven photocatalytic reactions. The absorption edges of the semiconductor photocatalysts BO-400 and BO-400@PAN-140 are 440 and 630 nm. The absorptive band edge of BO-400@PAN-140 is red-shifted relative to that of BO-400 indicating that the addition of the polymer inhibits the partial transformation of bismuth oxycarbonate.[40] Such heterojunction photocatalysts can enhance the visible light absorption while narrowing its bandgap, maximising the number of photogenerated carriers.

The bandgap structure strongly influences the photocatalytic activity; it can be evaluated by Tuac's equation:

$$\alpha h\nu = A(h\nu - E_g)^{n/2} \quad (2)$$

where α, h, ν, A, and E_g are the absorption coefficient, Planck constant, light frequency, empirically determined constant, and the bandgap energy, respectively. The value of n, which depends on the transition characteristics of the semiconductor, is taken

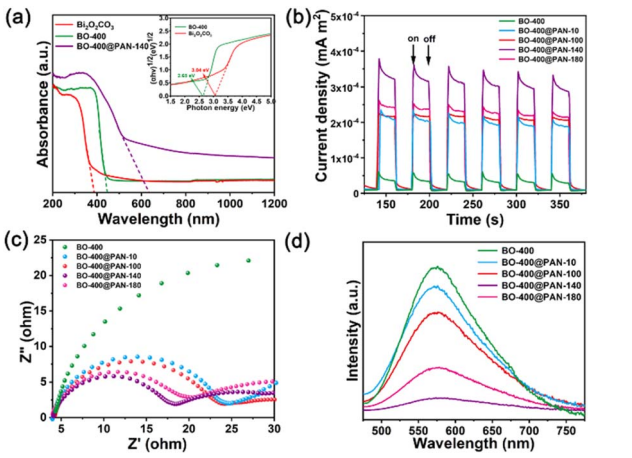

Fig. 5 (a) UV-vis diffuse reflectance spectra of $Bi_2O_2CO_3$, BO-400, and BO-400@PAN-140 composites. (a) Tauc's plots of $Bi_2O_2CO_3$ and BO-400. (b) Transient photocurrent response (TPR) curves of BO-400@PAN-*Y*. (c) Electrochemical impedance spectroscopy (EIS) spectra of BO-400 and BO-400@PAN-140. (d) PL spectra of BO-400 and BO-400@PAN-*Y* composites.

as 4 in this context based on the indirect transformation of $Bi_2O_2CO_3$ to α-Bi_2O_3.[41] The band gaps (Fig. 5a1) of α-Bi_2O_3 and $Bi_2O_2CO_3$ were determined to be 2.96 and 2.65 eV.

The band edge positions of $Bi_2O_2CO_3$ and α-Bi_2O_3 can be predicted theoretically based on electronegativity. The valence band (VB) and conduction band (CB) potentials of the as-prepared, charge-neutral photocatalysts were determined as follows.[41,42]

$$E_{VB} = X - E_e + 0.5E_g \quad (3)$$

$$E_{CB} = E_{VB} - E_g \quad (4)$$

where E_g is the bandgap energy of the semiconductor; E_{VB} corresponds to the valence band edge potential; E_{CB} corresponds to the conduction band edge potential; X is the absolute electronegativity of the semiconductor, which is the geometric mean of the absolute electronegativity of the constituent atoms (X for $Bi_2O_2CO_3$ and α-Bi_2O_3 is 6.36 and 6.23 eV, respectively);[43] and E_e is the energy of free electrons (~4.5 eV).

Based on the above formula and data, the VB and CB edge potentials of $Bi_2O_2CO_3$ are estimated to be 3.24 and 0.28 eV, respectively, while the VB and CB edge potentials of α-Bi_2O_3 are estimated to be 3.05 and 0.40 eV. To further validate this inferred band structure, the valence band edges of $Bi_2O_2CO_3$ and α-Bi_2O_3 were characterised based on the valence-band XPS (VB-XPS) measurements. As shown in Fig. S10,† the valence band edges of original $Bi_2O_2CO_3$ and α-Bi_2O_3 are 3.22 eV and 3.03 eV, which are comparable to the results of the theoretical calculation. These energy band structures are also presented in Table S1.†

The charge transfer and separation efficiency of photogenerated electron–hole pairs are crucial to photocatalytic performance, as reflected by the transient photocurrent response (TPR).[44] The TPR profiles shown in Fig. 5b demonstrate that BO-400 and BO-400@PAN-*Y* were stable in response to each irradiation, while also confirming that the photocurrent response of BO-400@PAN-*Y* is higher than that of BO-400, which may be derived from the formation of the $Bi_2O_2CO_3$/α-Bi_2O_3 p–n heterojunction. The existence of this heterojunction can also improve both the transferability and separability of the photogenerated carriers. BO-400@PAN-140 exhibited the highest TPR; irradiation by a medical cold light source generated a rapid photocurrent that reached a steady-state over a short interval. Electrochemical impedance spectroscopy (EIS) was employed to further validate interfacial charge transfer behaviour.[45] As illustrated in Fig. 5c, the arch radius of the heterojunction catalyst BO-400@PAN-140 impedance curve is smaller than that of BO-400, BO-400@PAN-10, BO-400@PAN-100, and BO-400@PAN-180, further demonstrating that the interaction between α-Bi_2O_3 and $Bi_2O_2CO_3$ can effectively reduce the charge transfer resistance at the phase interface. These findings confirm that BO-400@PAN-140 possesses significantly improved interface charge transfer and electron–hole pair separation efficiencies. The separation and recombination of photogenerated carriers can be further detected from the photoluminescence (PL) spectra.[46] The PL spectra of BO-400 and BO-400@PAN-140 photocatalysts are presented in Fig. 5d, based on an excitation wavelength at 375 nm. BO-400 exhibits a strong emission at 530 nm due to carrier recombination under optical radiation. Relative to BO-400, the BO-400@PAN-*Y* photocatalysts exhibited a noticeably quenched PL signal, indicating that the formation of α-Bi_2O_3 and $Bi_2O_2CO_3$ heterojunction inhibits the direct recombination of photogenerated electrons and holes. The PL intensity of the BO-400@PAN-*Y* nanocomposites decreases as the ratio of PAN is reduced, corresponding to enhanced electron mobility in the conjugated system. In summary, the photogenerated electron/hole between $Bi_2O_2CO_3$ and α-Bi_2O_3 favors electron transfer and, by extension, the photocatalytic degradation rate.

Possible degradation mechanism

To better characterise the photocatalytic mechanism of BO-400@PAN-140, a series of free radical trapping experiments were conducted to systematically identify the active radicals involved in the decomposition of organic pollutants. L-Ascorbic acid (L-AA), ethylene diamine tetraacetic acid (EDTA), and *tert*-butyl alcohol (TBA) were employed as the scavenging reagents to quench peroxide radicals ($^{\bullet}O_2^-$), holes (h^+), and hydroxyl radicals ($^{\bullet}OH$), respectively.[47] As shown in Fig. S11,† TC degradation was almost unaffected after the addition of 1 mM L-AA. In contrast, the addition of TBA and EDTA significantly affected the degradation of TC, indicating that $^{\bullet}OH$ and h^+ played a major role in the removal of TC over α-Bi_2O_3/$Bi_2O_2CO_3$ heterojunction catalysts.

EPR (Electron Paramagnetic Resonance) experiments were conducted to further validate the active species involved in the photodegradation of TC over BO-400@PAN-140. The capture agents for h^+ and $^{\bullet}OH$ were TEMPO and DMPO, respectively.[19] As indicated in Fig. 6a, the signal intensity of h^+ following 5 and 10 min of light exposure is weaker than without any exposure, implying that the photocatalyst is conducive to the separation and migration of photogenerated electrons/holes under irradiation. Fig. 6b indicates the absence of the $^{\bullet}OH$ signal under dark conditions. However, the signal intensity of $^{\bullet}OH$ was shown to gradually increase with the increasing light irradiation.[48] BO-400@PAN-140 significantly enhances molecular oxygen activation to generate $^{\bullet}OH$, which is derived from strong interactions engendered in the Bi–N bonds at the interface of the photocatalyst and PAN additive.[49,50] These EPR results

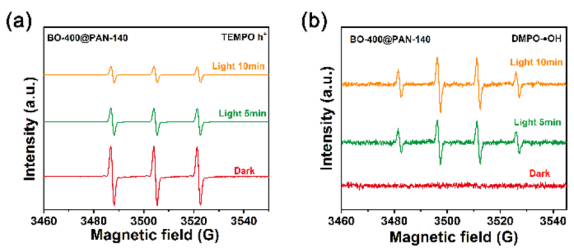

Fig. 6 Electron paramagnetic resonance (EPR) spectra of the (a) DMPO-h^+, and (b) DMPO-$^{\bullet}OH$ adducts were recorded with the BO-400@PAN-140 under the dark and light irradiation.

further validate the generation of h^+ and $^{\bullet}OH$ radicals under visible light, which is also consistent with the results of radical trapping experiments.

Possible tetracycline degradation pathway

HPLC-MS results highlight the key intermediate products and possible reaction pathways for photocatalytic degradation for TC over BO-400@PAN-140 (the corresponding molecular formulas and structure of which are presented in Fig. S12†). Using insights from the relevant literature and detected intermediates, Fig. 7 illustrates two possible TC degradation pathways.[51] The active species, which consist of $^{\bullet}OH$, and h^+, can effectively attack partially unstable TC groups including amine, double-bond, and phenolic groups, resulting in the cleavage of such functional groups as the photocatalytic reaction progresses.[52] The base peak chromatogram of untreated solution exhibits its main peak at $m/z = 445$, corresponding to the tetracycline molecule. Pathway I is characterised by a methyl of the amino group on T1 gradually colliding into the minor molecule T2 ($m/z = 431$) by h^+ attack of the methyl and aldehyde species. Subsequent $^{\bullet}OH$ degradation of the methyl species on the tertiary amine leads to the formation of T5 ($m/z = 417$).[53] The transformation from T5 to T6 ($m/z = 345$) is driven by the cleavage of the acylamido group and open-ring reactions.[54] Pathway II is characterised by the attack of T1 ($m/z = 445$) by $^{\bullet}OH$ (formed from H_2O) to produce the product T3 ($m/z = 428$).[55] Given its high electron density, the cleavage of the C–N bond can be attributed to the formation of the intermediate product T4 ($m/z = 399$). T7 and T8 were transformed into small organic molecular byproducts ($m/z = 118$, $m/z = 164$, and $m/z = 136$) following a series of open-ring reactions and the forfeiture of specific groups. These small organics were ultimately converted to CO_2 and H_2O by an attack of $^{\bullet}OH$ and h^+.

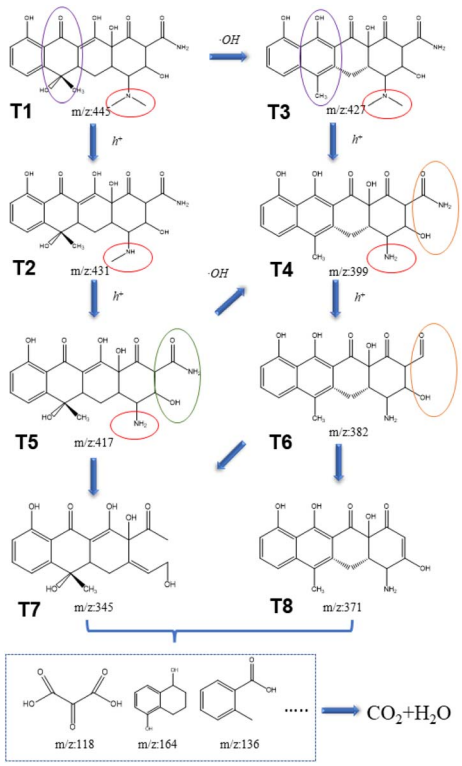

Fig. 7 Intermediate products and proposed degradation pathway of TC.

The relative band edge positions of the two materials determine the direction of migration of photogenerated electrons and holes on the p–n heterojunction photocatalyst. The likely mechanism for the enhancement of photocatalytic degradation activity follows from the preceding analysis and energy band calculations.[56,57] In contrast with the CB and VB positions of pure $Bi_2O_2CO_3$ and α-Bi_2O_3, the p–n heterojunction photocatalyst exhibits nested band energy levels (left of Scheme 2), which is unfavourable for the parting and transmission of photogenerated carriers. The Fermi energy level (E_f) of α-Bi_2O_3 is close to its valence band, while $Bi_2O_2CO_3$ approximates its conduction band.[58,59] The CB and VB locations of α-Bi_2O_3 and $Bi_2O_2CO_3$ are shifted as a result of the formation of the p–n heterojunction structure. The E_f of p-type α-Bi_2O_3 would increase, while that of n-type $Bi_2O_2CO_3$ decrease, ultimately reaching a new equilibrium to form a new staggered band structure.

Following this transformation of the energy band structure, the conduction band position of $Bi_2O_2CO_3$ is lower than that of α-Bi_2O_3. This optimised energy band structure favours the departure and migration of photocatalytic carriers. The inner electron field forms at the interface of n-type $Bi_2O_2CO_3$ and p-type α-Bi_2O_3. Consistent with the staggered band structure of the composite photocatalyst, a promising photocatalytic degradation mechanism is proposed—as illustrated to the right of Scheme 2. Under visible-light irradiation, photogenerated carriers emerge from the α-Bi_2O_3 and $Bi_2O_2CO_3$ phases. The optimised energy band structure is conducive to the rapid transfer of photogenerated electrons from the α-Bi_2O_3 conduction band to the $Bi_2O_2CO_3$ conduction band.

As electrons migrate between the conduction bands of two components, the holes in the valence band of $Bi_2O_2CO_3$ will rapidly transfer to that of α-Bi_2O_3, ultimately forming a p–n heterojunction between α-Bi_2O_3 and $Bi_2O_2CO_3$ to effectively separate electron–hole pairs. Simultaneously, the heterojunction-induced electric field inhibits the recombination of the electrons and holes at the interface of the two semiconductors. The charges migrate to the surface of the catalysts with the dissolved oxygen and OH^- in water, enabling the continuous formation of essential active groups. The conduction band potentials of $Bi_2O_2CO_3$ and α-Bi_2O_3 are both higher than the redox potential of $O_2/^{\bullet}O_2^-$(−0.33 eV).[60] Therefore, dissolved oxygen in water cannot be reduced to $^{\bullet}O_2^-$, having gained electrons in the conduction band.

The redox potential of O_2/H_2O_2 is 0.695 eV,[61,62] which is higher than the CB potential of $Bi_2O_2CO_3$. Consequently, O_2 can initially be reduced to H_2O_2, further enabling the capture of electrons to form $^{\bullet}OH$. The α-Bi_2O_3 possesses a higher valence band potential than the redox potential of $OH^-/^{\bullet}OH$ (2.40 eV).[63] Holes in the valence band of α-Bi_2O_3 oxidise OH^- to $^{\bullet}OH$, while also migrating to the surface of the catalyst to promote the enhanced oxidation of TC. Together, $^{\bullet}OH$ and h^+ function as

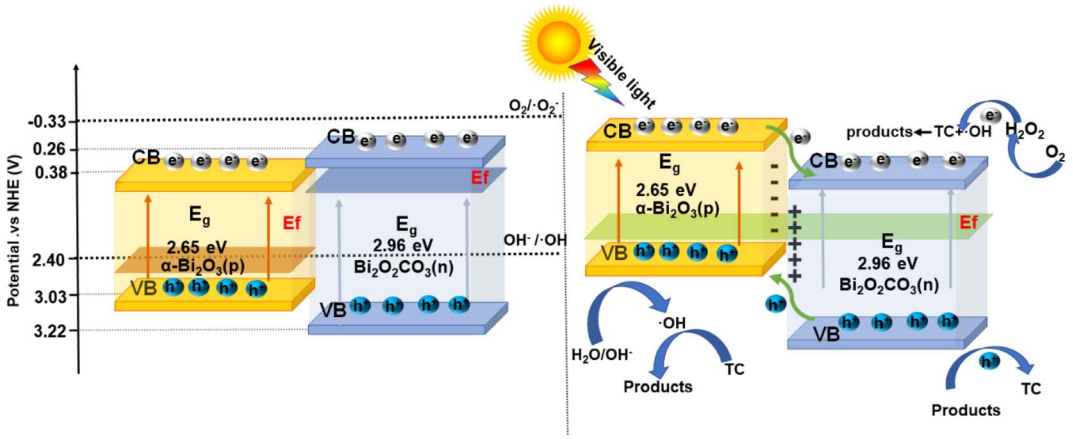

Scheme 2 A possible mechanism for pollutant degradation and electron flow with the BO-400@PAN-140 photocatalyst.

strong oxidizing species for the degradation of TC contaminant molecules on the surface of the photocatalyst and the superior degradation performance (under visible-light irradiation) of the p–n heterojunction photocatalyst relative to that of a single $Bi_2O_2CO_3$ and α-Bi_2O_3 originates from its numerous mechanistic advantages.

Conclusions

A α-Bi_2O_3/$Bi_2O_2CO_3$ p–n heterojunction photocatalyst has been successfully synthesised *via* a facile annealing method. The α-Bi_2O_3/$Bi_2O_2CO_3$ p–n heterojunction demonstrated excellent photocatalytic performance for the degradation both of antibiotic (TC) and dye (RhB) contaminants, which can be attributed to the existence of a suitable energy band structure enabling the rapid separation of photogenerated carriers. Following only 60 min of visible-light irradiation, TC degradation efficiency of 98.2% was achieved using the BO-400@PAN-140 photocatalyst. This degradation efficiency was maintained above 95% after the completion of five cycles. Free radical scavenging tests and electron paramagnetic resonance (EPR) results demonstrated h^+ and ˙OH radicals as the primary active species in photocatalytic degradation. The HPLC-MS results also indicated that the TC molecules can be effectively decomposed through two pathways. For this reason, our proposed methodology for the synthesis of α-Bi_2O_3/$Bi_2O_2CO_3$-based p–n heterojunctions with high contaminant photodegradation efficiency can make a significant impact on improving the readiness of photocatalytic water purification technologies.

Author contributions

Baikang Zhu: writing—review & editing, project administration, funding acquisition. Debin Song: conceptualization, methodology, visualization, writing—original draft. Lihui Chen: writing—review & editing. Qingguo Chen: writing—review & editing. Chunyang Zhai: writing—review & editing. Bohong Wang: writing—review & editing. Jiří Jaromír Klemešf: writing—review & editing, funding acquisition. Hengcong Tao: conceptualization, methodology, writing—review & editing, supervision, funding acquisition. All authors have read and agreed to the published version of the manuscript.

Conflicts of interest

The authors declare no competing financial interest.

Acknowledgements

This work was financially supported by: the NSFC-Zhejiang Joint Fund for Integration of Industrialization and Diversification (U1809214); the National Natural Science Foundation of China (No. 22005269); the Natural Science Foundation of Zhejiang Province (No. LQ21B030007); Zhejiang Province Public Welfare Technology Research Project (No. LGF20D060001); Zhejiang Province Public Welfare Technology Research Project (No. LGF22D060003); Science and Technological program of Ningbo (Grant 2021S136); and EU project "Sustainable Process Integration Laboratory—SPIL", project No. CZ.02.1.01/0.0/0.0/15_003/0000456 funded by EU "CZ Operational Programme Research, Development and Education", Priority 1: Strengthening capacity for quality research.

References

1 M. Zulfiqar, S. Sufian, A. Bahadar, N. Lashari, N. E. Rabat and N. Mansor, Surface-fluorination of TiO_2 photocatalysts for remediation of water pollution: a review, *J. Cleaner Prod.*, 2021, **317**, 128354.

2 P. E. Spector, S. Fox, L. M. Penney, K. Bruursema, A. Goh and S. Kessler, The dimensionality of counterproductivity: Are all counterproductive behaviors created equal?, *J. Vocat. Behav.*, 2006, **68**, 446–460.

3 Z. J. Chen, H. Guo, H. Y. Liu, C.-G. Niu, D.-W. Huang, Y. Y. Yang, C. Liang, L. Li and J. C. Li, Construction of dual S-scheme Ag_2CO_3/$Bi_4O_5I_2$/g-C_3N_4 heterostructure photocatalyst with enhanced visible-light photocatalytic

degradation for tetracycline, *Chem. Eng. J.*, 2022, **438**, 135471.

4 A. L. Srivastav, N. Patel and V. K. Chaudhary, Disinfection by-products in drinking water: Occurrence, toxicity and abatement, *Environ. Pollut.*, 2020, **267**, 115474.

5 Y. Liang, W. Xu, J. Fang, Z. Liu, D. Chen, T. Pan, Y. Yu and Z. Fang, Highly dispersed bismuth oxide quantum dots/graphite carbon nitride nanosheets heterojunctions for visible light photocatalytic redox degradation of environmental pollutants, *Appl. Catal. B Environ.*, 2021, **295**, 120279.

6 X. Li, J. Yu and M. Jaroniec, Hierarchical photocatalysts, *Chem. Soc. Rev.*, 2016, **45**, 2603–2636.

7 P. Xu, M. Chen, G. Zeng, D. Huang, C. Lai, Z. Wang, M. Yan, Z. Huang, X. Gong, B. Song, T. Li and A. Duan, Effects of multi-walled carbon nanotubes on metal transformation and natural organic matters in riverine sediment, *J. Hazard. Mater.*, 2019, **374**, 459–468.

8 S. Tian, C. Zhang, D. Huang, R. Wang, G. Zeng, M. Yan, W. Xiong, C. Zhou, M. Cheng, W. Xue, Y. Yang and W. Wang, Recent progress in sustainable technologies for adsorptive and reactive removal of sulfonamides, *Chem. Eng. J.*, 2020, **389**, 123423.

9 M. Yu, J. Wang, L. Tang, C. Feng, H. Liu, H. Zhang, B. Peng, Z. Chen and Q. Xie, Intimate coupling of photocatalysis and biodegradation for wastewater treatment: mechanisms, recent advances and environmental applications, *Water Res.*, 2020, **175**, 115673.

10 P. Yang, C. Chen, D. Wang, H. Ma, Y. Du, D. Cai, X. Zhang and Z. Wu, Kinetics, reaction pathways, and mechanism investigation for improved environmental remediation by 0D/3D CdTe/Bi_2WO_6 Z-scheme catalyst, *Appl. Catal. B Environ.*, 2021, **285**, 119877.

11 K. Qin, Q. Zhao, H. Yu, X. Xia, J. Li, S. He, L. Wei and T. An, A review of bismuth-based photocatalysts for antibiotic degradation: Insight into the photocatalytic degradation performance, pathways and relevant mechanisms, *Environ. Res.*, 2021, **199**, 111360.

12 K. K. Bera, R. Majumdar, M. Chakraborty and S. K. Bhattacharya, Phase control synthesis of alpha, beta and α/β Bi_2O_3 hetero-junction with enhanced and synergistic photocatalytic activity on degradation of toxic dye, Rhodamine-B under natural sunlight, *J. Hazard. Mater.*, 2018, **352**, 182–191.

13 W. An, S. Hu, T. Yang, H. Wang, J. Hu, W. Cui and Y. Liang, Oxygen vacancies enhance Fe-doped BiOCl photocatalysis-Fenton synergy degradation of phenol, *Mater. Lett.*, 2022, **322**, 132466.

14 G. Yang, Y.-A. Zhu, Y. Liang, J. Yang, K. Wang, Z. Zeng, R. Xu and X. Xie, Crystal defect-mediated {010} facets of Bi_2MoO_6 nanosheets for removal of TC: Enhanced mechanism and degradation pathway, *Appl. Surf. Sci.*, 2021, **539**, 148038.

15 H. Zhao, G. Li, F. Tian, Q. Jia, Y. Liu and R. Chen, g-C_3N_4 surface-decorated $Bi_2O_2CO_3$ for improved photocatalytic performance: Theoretical calculation and photodegradation of antibiotics in actual water matrix, *Chem. Eng. J.*, 2019, **366**, 468–479.

16 X. Ji, Q. Wang, J. Lu and D. Zhang, Construction of a novel $Ca_2Bi_2O_5$/α-Bi_2O_3 semiconductor heterojunction for enhanced visible photocatalytic application, *Ceram. Int.*, 2020, **46**, 13630–13640.

17 L. Wang, H. Yin, S. Wang, J. Wang and S. Ai, Ni^{2+}-assisted catalytic one-step synthesis of Bi/BiOCl/$Bi_2O_2CO_3$ heterojunction with enhanced photocatalytic activity under visible light, *Appl. Catal. B Environ.*, 2022, **305**, 121039.

18 H. Tao, Q. Fan, T. Ma, S. Liu, H. Gysling, J. Texter, F. Guo and Z. Sun, Two-dimensional materials for energy conversion and storage, *Prog. Mater. Sci.*, 2020, **111**, 100637.

19 Y. Lu, Y. Huang, Y. Zhang, J. Cao, H. Li, C. Bian and S. C. Lee, Oxygen vacancy engineering of Bi_2O_3/$Bi_2O_2CO_3$ heterojunctions: Implications of the interfacial charge transfer, NO adsorption and removal, *Appl. Catal. B Environ.*, 2018, **231**, 357–367.

20 Y. Cui, X. Zhang, R. Guo, H. Zhang, B. Li, M. Xie, Q. Cheng and X. Cheng, Construction of Bi_2O_3/g-C_3N_4 composite photocatalyst and its enhanced visible light photocatalytic performance and mechanism, *Sep. Purif. Technol.*, 2018, **203**, 301–309.

21 H. Zhou, S. Zhong, M. Shen and Y. Yao, Composite soft template-assisted construction of a flower-like β-Bi_2O_3/$Bi_2O_2CO_3$ heterojunction photocatalyst for the enhanced simulated sunlight photocatalytic degradation of tetracycline, *Ceram. Int.*, 2019, **45**, 15036–15047.

22 C. W. Kim, S. J. Yeob, H.-M. Cheng and Y. S. Kang, A selectively exposed crystal facet-engineered TiO_2 thin film photoanode for the higher performance of the photoelectrochemical water splitting reaction, *Energy Environ. Sci.*, 2015, **8**, 3646–3653.

23 A. C. Gandhi, C. Y. Lai, K. T. Wu, P. Ramacharyulu, V. B. Koli, C. L. Cheng, S. C. Ke and S. Y. Wu, Phase transformation and room temperature stabilization of various Bi_2O_3 nano-polymorphs: effect of oxygen-vacancy defects and reduced surface energy due to adsorbed carbon species, *Nanoscale*, 2020, **12**, 24119–24137.

24 A. Hernández-Gordillo, J. C. Medina, M. Bizarro, R. Zanella, B. M. Monroy and S. E. Rodil, Photocatalytic activity of enlarged microrods of α-Bi_2O_3 produced using ethylenediamine-solvent, *Ceram. Int.*, 2016, **42**, 11866–11875.

25 W. He, Y. Sun, G. Jiang, H. Huang, X. Zhang and F. Dong, Activation of amorphous Bi_2WO_6 with synchronous Bi metal and Bi_2O_3 coupling: Photocatalysis mechanism and reaction pathway, *Appl. Catal. B Environ.*, 2018, **232**, 340–347.

26 Y. Xu, H. Zhang, Q. Liu, J. Liu, R. Chen, J. Yu, J. Zhu, R. Li and J. Wang, Surface hybridization of π-conjugate structure cyclized polyacrylonitrile and radial microsphere shaped TiO_2 for reducing U(VI) to U(IV), *J. Hazard. Mater.*, 2021, **416**, 125812.

27 X. Xiao, S. Tu, C. Zheng, H. Zhong, X. Zuo and J. Nan, L-Asparagine-assisted synthesis of flower-like β-Bi_2O_3 and its photocatalytic performance for the degradation of 4-phenylphenol under visible-light irradiation, *RSC Adv.*, 2015, **5**, 74977–74985.

28 B. Lei, W. Cui, J. Sheng, H. Wang, P. Chen, J. Li, Y. Sun and F. Dong, Synergistic effects of crystal structure and oxygen vacancy on Bi_2O_3 polymorphs: intermediates activation, photocatalytic reaction efficiency, and conversion pathway, *Sci. Bull.*, 2020, **65**, 467–476.

29 Z. Wang, H. Wang, Z. Zeng, G. Zeng, P. Xu, R. Xiao, D. Huang, X. Chen, L. He, C. Zhou, Y. Yang, Z. Wang, W. Wang and W. Xiong, Metal-organic frameworks derived $Bi_2O_2CO_3$/porous carbon nitride: A nanosized Z-scheme systems with enhanced photocatalytic activity, *Appl. Catal. B Environ.*, 2020, **267**, 118700.

30 B. Li, L.-C. Nengzi, R. Guo, Y. Cui, Y. Zhang and X. Cheng, Novel synthesis of Z-scheme α-Bi_2O_3/g-C_3N_4 composite photocatalyst and its enhanced visible light photocatalytic performance: Influence of calcination temperature, *Chin. Chem. Lett.*, 2020, **31**, 2705–2711.

31 Z. Liu, J. Huang, B. Shao, H. Zhong, Q. Liang, Q. He, T. Wu, Y. Pan, Z. Peng, X. Yuan, Y. Liu and C. Zhao, In-situ construction of 2D/1D $Bi_2O_2CO_3$ nanoflake/S-doped g-C_3N_4 hollow tube hierarchical heterostructure with enhanced visible-light photocatalytic activity, *Chem. Eng. J.*, 2021, **426**, 130767.

32 F. Wang, Y. Song, Q. He, C. Zhang, J. Lai, S. Zhan and F. Zhou, Performance tuning and optimisation of 2D–2D-like g-C_3N_4 modified $Bi_2O_2CO_3$ n–n homotypic heterojunction as an inactivating photocatalytic material, *J. Environ. Chem. Eng.*, 2021, **9**, 106176.

33 A. H. Zahid and Q. Han, A review on the preparation, microstructure, and photocatalytic performance of Bi_2O_3 in polymorphs, *Nanoscale*, 2021, **13**, 17687–17724.

34 Z. Guan, X. Li, Y. Wu, Z. Chen, X. Huang, D. Wang, Q. Yang, J. Liu, S. Tian, X. Chen and H. Zhao, AgBr nanoparticles decorated 2D/2D GO/Bi_2WO_6 photocatalyst with enhanced photocatalytic performance for the removal of tetracycline hydrochloride, *Chem. Eng. J.*, 2021, **410**, 128283.

35 C. Lai, F. Xu, M. Zhang, B. Li, S. Liu, H. Yi, L. Li, L. Qin, X. Liu, Y. Fu, N. An, H. Yang, X. Huo, X. Yang and H. Yan, Facile synthesis of CeO_2/carbonate doped $Bi_2O_2CO_3$ Z-scheme heterojunction for improved visible-light photocatalytic performance: Photodegradation of tetracycline and photocatalytic mechanism, *J. Colloid Interface Sci.*, 2021, **588**, 283–294.

36 X. Ma, K. Chen, B. Niu, Y. Li, L. Wang, J. Huang, H. She and Q. Wang, Preparation of $BiOCl_{0.9}I_{0.1}$/β-Bi_2O_3 composite for degradation of tetracycline hydrochloride under simulated sunlight, *Chin. J. Catal.*, 2020, **41**, 1535–1543.

37 J.-c. Shen, H.-y. Zeng, C.-r. Chen and S. Xu, Novel plasmonic p–n heterojunction Ag-Ag_2CO_3/$Bi_2Sn_2O_7$ photocatalyst for Cr(VI) reduction, *J. Taiwan Inst. Chem. Eng.*, 2021, **120**, 106–115.

38 Q. Chen, C. Yuan and C. Zhai, Label-free photoelectrochemical sensor based on 2D/2D $ZnIn_2S_4$/g-C_3N_4 heterojunction for the efficient and sensitive detection of bisphenol A, *Chin. Chem. Lett.*, 2022, **33**, 983–986.

39 S. Adhikari, S. Mandal and D.-H. Kim, 1D/2D constructed Bi_2S_3/$Bi_2O_2CO_3$ direct Z-Scheme heterojunction: A versatile photocatalytic material for boosted photodegradation, photoreduction and photoelectrochemical detection of water-based contaminants, *J. Hazard. Mater.*, 2021, **418**, 126263.

40 C. Zhou, C. Lai, D. Huang, G. Zeng, C. Zhang, M. Cheng, L. Hu, J. Wan, W. Xiong, M. Wen, X. Wen and L. Qin, Highly porous carbon nitride by supramolecular preassembly of monomers for photocatalytic removal of sulfamethazine under visible light driven, *Appl. Catal. B Environ.*, 2018, **220**, 202–210.

41 T. Zhao, J. Zai, M. Xu, Q. Zou, Y. Su, K. Wang and X. Qian, Hierarchical $Bi_2O_2CO_3$ microspheres with improved visible-light-driven photocatalytic activity, *CrystEngComm*, 2011, **13**, 4010–4017.

42 Y. Huang, W. Wang, Q. Zhang, J. Cao, R. Huang, W. Ho and S. C. Lee, In situ fabrication of α-Bi_2O_3/$(BiO)_2CO_3$ nanoplate heterojunctions with tunable optical property and photocatalytic activity, *Sci. Rep.*, 2016, **6**, 23435.

43 L. Chen, S. Yin, S. Luo, R. Huang, Q. Zhang, T. Hong and P. Au, $Bi_2O_2CO_3$/BiOI photocatalysts with heterojunctions highly efficient for visible-light treatment of dye-containing wastewater, *Ind. Eng. Chem. Res.*, 2012, **51**, 6760–6768.

44 X. Lian, W. Xue, S. Dong, E. Liu, H. Li and K. Xu, Construction of S-scheme Bi_2WO_6/g-C_3N_4 heterostructure nanosheets with enhanced visible-light photocatalytic degradation for ammonium dinitramide, *J. Hazard. Mater.*, 2021, **412**, 125217.

45 X. Ruan, X. Wen, D. Liang and Y. Hu, Hierarchically peony-analogous bismuth tungstate with oxygen vacancies for enhanced photocatalytic degradation of phenolic compounds, *J. Clean. Prod.*, 2021, **324**, 129287.

46 H. Jiang, Q. Wang, P. Chen, H. Zheng, J. Shi, H. Shu and Y. Liu, Photocatalytic degradation of tetracycline by using a regenerable (Bi)BiOBr/rGO composite, *J. Clean. Prod.*, 2022, **339**, 130771.

47 J. Zhang, B. Jing, Z. Tang, Z. Ao, D. Xia, M. Zhu and S. Wang, Experimental and DFT insights into the visible-light driving metal-free C_3N_5 activated persulfate system for efficient water purification, *Appl. Catal. B Environ.*, 2021, **289**, 120023.

48 J. He, J. Yang, F. Jiang, P. Liu and M. Zhu, Photo-assisted peroxymonosulfate activation via 2D/2D heterostructure of Ti_3C_2/g-C_3N_4 for degradation of diclofenac, *Chemosphere*, 2020, **258**, 127339.

49 L. Zhang, L. Han, H. Liu, X. Liu and J. Luo, Potential-cycling synthesis of single platinum atoms for efficient hydrogen evolution in neutral media, *Angew. Chem., Int. Ed.*, 2017, **56**, 13694–13698.

50 L. Jin, B. Zhu, X. Wang, L. Zhang, D. Song, J. Guo and H. Tao, Facile synthesis of the amorphous carbon coated Fe-N-C nanocatalyst with efficient activity for oxygen reduction reaction in acidic and alkaline media, *Materials*, 2020, **13**, 4551.

51 H. Fattahimoghaddam, T. Mahvelati-Shamsabadi and B. K. Lee, Efficient Photodegradation of Rhodamine B and Tetracycline over Robust and Green g-C_3N_4 Nanostructures: Supramolecular Design, *J. Hazard. Mater.*, 2021, **403**, 123703.

52 Y. Deng, L. Tang, G. Zeng, J. Wang, Y. Zhou, J. Wang, J. Tang, L. Wang and C. Feng, Facile fabrication of mediator-free Z-scheme photocatalyst of phosphorous-doped ultrathin graphitic carbon nitride nanosheets and bismuth vanadate composites with enhanced tetracycline degradation under visible light, *J. Colloid Interface Sci.*, 2018, **509**, 219–234.

53 J. Cao, Z. Yang, W. Xiong, Y. Zhou, Y. Peng, X. Li, C. Zhou, R. Xu and Y. Zhang, One-step synthesis of Co-doped UiO-66 nanoparticle with enhanced removal efficiency of tetracycline: Simultaneous adsorption and photocatalysis, *Chem. Eng. J.*, 2018, **353**, 126–137.

54 N. Tian, X. Tian, Y. Nie, C. Yang, Z. Zhou and Y. Li, Biogenic manganese oxide: An efficient peroxymonosulfate activation catalyst for tetracycline and phenol degradation in water, *Chem. Eng. J.*, 2018, **352**, 469–476.

55 V. Maroga Mboula, V. Hequet, Y. Gru, R. Colin and Y. Andres, Assessment of the efficiency of photocatalysis on tetracycline biodegradation, *J. Hazard. Mater.*, 2012, **209–210**, 355–364.

56 S. Li, C. Wang, Y. Liu, B. Xue, W. Jiang, Y. Liu, L. Mo and X. Chen, Photocatalytic degradation of antibiotics using a novel $Ag/Ag_2S/Bi_2MoO_6$ plasmonic p–n heterojunction photocatalyst: Mineralization activity, degradation pathways and boosted charge separation mechanism, *Chem. Eng. J.*, 2021, **415**, 128991.

57 J. Nie, G. Zhu, W. Zhang, J. Gao, P. Zhong, X. Xie, Y. Huang and M. Hojamberdiev, Oxygen vacancy defects-boosted deep oxidation of NO by β-$Bi_2O_3/CeO_{2-\delta}$ p–n heterojunction photocatalyst in situ synthesized from $Bi/Ce(CO_3)(OH)$ precursor, *Chem. Eng. J.*, 2021, **424**, 130327.

58 S. Li, K. Xu, S. Hu, W. Jiang, J. Zhang, J. Liu and L. Zhang, Synthesis of flower-like Ag_2O/BiOCOOH p–n heterojunction with enhanced visible light photocatalytic activity, *Appl. Surf. Sci.*, 2017, **397**, 95–103.

59 H. Huang, X. Han, X. Li, S. Wang, P. K. Chu and Y. Zhang, Fabrication of multiple heterojunctions with tunable visible-light-active photocatalytic reactivity in BiOBr-BiOI full-range composites based on microstructure modulation and band structures, *ACS Appl. Mater. Interfaces*, 2015, **7**, 482–492.

60 F. Chang, W. Yan, X. Wang, S. Peng, S. Li and X. Hu, Strengthened photocatalytic removal of bisphenol a by robust 3D hierarchical n-p heterojunctions $Bi_4O_5Br_2$-MnO_2 via boosting oxidative radicals generation, *Chem. Eng. J.*, 2022, **428**, 131223.

61 C. Zheng, C. Cao and Z. Ali, In situ formed $Bi/BiOBr_xI_{1-x}$ heterojunction of hierarchical microspheres for efficient visible-light photocatalytic activity, *Phys. Chem. Chem. Phys.*, 2015, **17**, 13347–13354.

62 I. Bibi, N. Nazar, M. Iqbal, S. Kamal, H. Nawaz, S. Nouren, Y. Safa, K. Jilani, M. Sultan, S. Ata, F. Rehman and M. Abbas, Green and eco-friendly synthesis of cobalt-oxide nanoparticle: Characterization and photo-catalytic activity, *Adv. Powder Technol.*, 2017, **28**, 2035–2043.

63 Q. Chen, H. Long, M. Chen, Y. Rao, X. Li and Y. Huang, In situ construction of biocompatible Z-scheme α-Bi_2O_3/$CuBi_2O_4$ heterojunction for NO removal under visible light, *Appl. Catal. B Environ.*, 2020, **272**, 119008.